

AD-A273 177

DOCUMENTATION PAGE

Form Approved
OMB No. 0704-0188

2



ion is estimated to average 1 hour per response, including the time for reviewing instructions, searching existing data sources, gathering and reviewing the collection of information. Send comments regarding this burden estimate or any other aspect of this collecting burden, including suggestions for reducing this burden, to Washington Headquarters Services, Directorate for Information Operations and Reports, 1215 Jefferson Avenue, Washington, DC 20540, and to the Office of Management and Budget, Paperwork Reduction Project (0704-0188), Washington, DC 20503.

2. REPORT DATE
23 Nov., 19933. REPORT TYPE AND DATES COVERED
Technical 8/1/92 - 7/31/93

4. TITLE AND SUBTITLE

"Synthesis and Characterization of Two-Dimensional Molecular Recognition Interfaces"

5. FUNDING NUMBERS

N00014-91-J-1991

6. AUTHOR(S)

R. M. Crooks, O. Chailapakul, C. B. Ross, L. Sun, and J. K. Schoer

7. PERFORMING ORGANIZATION NAME(S) AND ADDRESS(ES)

Department of Chemistry
University of New Mexico
Albuquerque, NM 871318. PERFORMING ORGANIZATION
REPORT NUMBER

10

9. SPONSORING / MONITORING AGENCY NAME(S) AND ADDRESS(ES)

Office of Naval Research
800 North Quincy Street
Arlington, VA 22217-500010. SPONSORING / MONITORING
AGENCY REPORT NUMBER

11. SUPPLEMENTARY NOTES

Prepared for publication in *Chemically Sensitive Interfaces* (ACS Symposium Series)

12a. DISTRIBUTION / AVAILABILITY STATEMENT

This document has been approved for public release and sale;
its distribution is unlimited.

12b. DISTRIBUTION CODE

N00179

13. ABSTRACT (Maximum 200 words)

We have used self-assembly chemistry to synthesize monolayer assemblies that function as molecular recognition interfaces. In the first part of this paper, we show that one-component self-assembled *n*-alkanethiol monolayers with carboxylic acid functionalized endgroups specifically adsorb vapor-phase acid-terminated molecules via hydrogen bonding or vapor-phase amine-terminate molecules via proton-transfer interactions. In the second part, we demonstrate that two-component monolayers, which consist of inert *n*-alkanethiol framework molecules and defect-inducing template molecules, can discriminate between solution-phase probe molecules based on their physical and chemical characteristics. By electrochemically etching the defects and then imaging the resulting surface by scanning tunneling microscopy the defect sites can be indirectly visualized.

93-29223

93 11 29 007



14. SUBJECT TERMS

PAGES

26

16. PRICE CODE

17. SECURITY CLASSIFICATION
OF REPORT

Unclassified

18. SECURITY CLASSIFICATION
OF THIS PAGE

Unclassified

19. SECURITY CLASSIFICATION
OF ABSTRACT

Unclassified

20. LIMITATION OF ABSTRACT

OFFICE OF NAVAL RESEARCH

GRANT N00014-91-J-1991

R&T Code s400x084yip01

Technical Report No. 10

Synthesis and Characterization of Two-Dimensional Molecular Recognition Interfaces

by

Richard M. Crooks, Orawon Chailapakul, Claudia B. Ross, Li Sun, and Jonathan K. Schoer

Prepared for Publication

in

Chemically Sensitive Interfaces

ACS Symposium Series

Department of Chemistry

University of New Mexico

Albuquerque, NM 87131

November 23, 1993

Reproduction in whole or in part is permitted for any purpose of the United States Government.

This document has been approved for public release and sale;
its distribution is unlimited.

Synthesis and Characterization of Two-Dimensional Molecular Recognition Interfaces

Richard M. Crooks, Orawon Chailapakul, Claudia B. Ross,
Li Sun, and Jonathan K. Schoer

Department of Chemistry, Texas A&M University,
College Station, TX 77843-3255

DTIC QUALITY INSPECTED 5

We have used self-assembly chemistry to synthesize monolayer assemblies that function as molecular recognition interfaces. In the first part of this paper, we show that one-component self-assembled *n*-alkanethiol monolayers with carboxylic acid functionalized endgroups specifically adsorb vapor-phase acid-terminated molecules via hydrogen bonding or vapor-phase amine-terminated molecules via proton-transfer interactions. In the second part, we demonstrate that two-component monolayers, which consist of inert *n*-alkanethiol framework molecules and defect-inducing template molecules, can discriminate between solution-phase probe molecules based on their physical and chemical characteristics. By electrochemically etching the defects and then imaging the resulting surface by scanning tunneling microscopy the defect sites can be indirectly visualized.

Molecular recognition is the selective binding of a probe molecule to a molecular receptor. This binding interaction relies on both non-covalent intermolecular chemical interactions, such as hydrogen bonding or van der Waals forces, and steric compatibility, such as size or shape inclusion. At present, a detailed understanding of molecular recognition phenomena is hindered primarily by two experimental problems. First, in many natural systems the receptor is a large, flexible, and complex molecule with many potential binding sites, and as a result it is difficult to quantify the specific types and magnitudes of interactions that lead to probe binding. Second, there are only a few analytical methods that are sufficiently specific and sensitive that they can be used for studying individual molecular interactions in bound probe/receptor complexes. These and other difficulties associated with natural systems have resulted in the synthesis of simpler model receptors and characterization of their interactions with probe molecules (1-3).

Two general strategies have been used for synthesizing and characterizing model receptors and their complexes with probe molecules. The first is based on interactions between small molecules: complexes formed between alkali-metal cations and cryptands or crown ethers are typical examples. This approach has the benefit of simplicity, and it is often possible to assign a recognition event to a particular type of intermolecular interaction. Polymeric receptors are better models

Accession For	
NTIS	CRA&I <input checked="" type="checkbox"/>
DTIC	TAB <input type="checkbox"/>
Unannounced <input type="checkbox"/>	
Justification	
By	
Distribution /	
Availability Codes	
Dist	Availability Codes
A-1	

for natural systems than those based on small molecules, but they are considerably more difficult to synthesize and characterize since it is difficult to design in rigidity or binding sites that have time-independent conformations. Four different strategies have been used for synthesizing polymeric receptors (1). The first approach involves copolymerization of small-molecule receptors with a polymeric backbone, which results in receptors randomly dispersed along the polymer backbone. The second approach involves grafting of monomeric receptors onto preformed polymers, which results in structures that are very similar to those obtained by copolymerization. The third strategy results in a higher degree of organization between individual receptors and is thus a better mimic of natural systems. In this case, the receptors are synthesized together into a single polymer, and this material is then copolymerized with a spectator backbone. Finally, an even higher degree of organization and cooperation between receptors can be achieved by binding the probe molecule to the receptors, which also contain polymerizable groups. When this receptor complex is copolymerized with a chemically inert polymeric backbone, it induces the formation of cavities whose size and shape are determined by the preformed receptor complex. If the polymer is rigidified by heavy crosslinking, the receptor cavity is locked into place even after removal of the target molecule (1).

Our interest is focused on surface-confined molecular recognition interfaces, but our work is guided by the principles discussed above for small molecule-small molecule interactions and small molecule-polymer interactions in homogeneous solutions. There are three key advantages to studying molecular recognition on surfaces: (1) rigid receptor sites can be designed; (2) the synthetic chemistry is simplified; (3) the surfaces can be attached to transducers, which greatly simplifies analysis and may transform the molecular recognition interface into a chemical sensor.

Our studies of molecular recognition phenomena are based on the concept illustrated in Scheme I. The basic chemical building blocks are model organic surfaces consisting of self-assembling monolayers (SAMs) of organomercaptans (4,5). It has previously been shown that *n*-alkanethiols spontaneously adsorb to Au from dilute solutions of ethanol and other nonaqueous solvents, and that the resulting SAMs assume a close-packed ($\sqrt{3} \times \sqrt{3}$)R30° overlayer structure on Au(111) and other textured Au surfaces. Spectroscopic studies indicate that monolayers formed from short organomercaptans are more disordered than those formed from longer-chain molecules, but all SAMs are quite robust in aqueous solutions and vapor-phase ambients. The best *n*-alkanethiol monolayers contain surprisingly few adventitious defect sites, even when prepared on ill-defined substrates (6-8).

As in all natural and synthetic approaches to molecular recognition, interactions in the surface-confined systems described here are promoted at the ambient/organic interface through both chemical and physical interactions. We have attempted to separate monolayer/molecule interaction phenomena into two distinct problems: one chemical and one physical; however, it is not possible at present to achieve this degree of segregation. Nevertheless, to the extent that it is possible, we view individual chemical and physical intermolecular interactions as tools that can be used in various combinations to synthesize more complex recognition apparatuses. The size and versatility of our "toolbox" is enhanced if we can quantitatively understand a range of monolayer/molecule interactions.

Results and Discussion

We have examined five types of chemical interactions that occur between monolayers and molecules: electrostatic binding, covalent linking, complexation interactions, proton transfer, and hydrogen bonding (9-14). These interactions are five of the six tools presently in our "toolbox"; the sixth is a physical recognition

strategy that is discussed later (6). We first consider two examples that illustrate chemical-interaction-based molecular recognition. The first example shows how carboxylic acid-terminated SAMs can be used to recognize vapor-phase acids via hydrogen bonding interactions. The second example shows how the same class of SAMs are used to recognize vapor-phase bases.

Chemical Interactions Between Probe Molecules and SAMs. In this section, we show that surface-confined monolayers of acid-functionalized organomercaptans interact with acidic or basic vapor-phase probe molecules by hydrogen-bonding (12) or proton-transfer (13) interactions, respectively. Hydrogen-bonding systems are typified by the interactions of *n*-alkanoic acids ($\text{CH}_3(\text{CH}_2)_n\text{COOH}$, $n = 0-14$) with Au surfaces modified by 3-mercaptopropionic acid ($\text{Au/HS}(\text{CH}_2)_2\text{COOH}$), as shown in Scheme II.

Hydrogen Bonding Interactions. Figure 1 shows FTIR external reflection spectroscopy (FTIR-ERS) data for $\text{Au/HS}(\text{CH}_2)_2\text{COOH}$ and $\text{Au/HS}(\text{CH}_2)_2\text{CH}_3$ surfaces after and before exposure to a saturated vapor of myristic acid, $\text{CH}_3(\text{CH}_2)_{12}\text{COOH}$. Prior to $\text{CH}_3(\text{CH}_2)_{12}\text{COOH}$ modification, the $\text{Au/HS}(\text{CH}_2)_2\text{COOH}$ spectrum, Figure 1b, indicates absorptions due to the acid C=O stretch and the enhanced $\alpha\text{-CH}_2$ scissors mode at 1722 and 1410 cm^{-1} , respectively (15-18). After dosing, the presence of a second surface-confined $\text{CH}_3(\text{CH}_2)_{12}\text{COOH}$ layer is confirmed by the appearance of the methyl C-H stretching vibration at 2964 cm^{-1} , the increased intensity of the methylene C-H stretching vibrations at 2929 and 2858 cm^{-1} , and the doubling of the intensity of the C=O stretching vibration at 1717 cm^{-1} (Figure 1a).

We performed control experiments by exposing a methylated SAM surface to vapor-phase *n*-alkanoic acids. The FTIR-ERS spectrum of a surface-confined monolayer of $\text{HS}(\text{CH}_2)_2\text{CH}_3$ is shown in Figure 1d. The peak at 2965 cm^{-1} is due to the asymmetric methyl C-H stretching vibration, and the peaks at 2935 and 2875 cm^{-1} are due to symmetric methyl C-H stretching vibrations. Other peaks attributable to hydrocarbon backbone modes are present at lower frequencies. The FTIR-ERS spectrum of the methyl surface after exposure to $\text{CH}_3(\text{CH}_2)_{12}\text{COOH}$, Figure 1c, is identical to the surface before acid dosing. This result clearly shows that only the acid-terminated SAM recognizes the vapor-phase acid.

Closer examination of the FTIR-ERS data presented in Figure 1 provides additional evidence for hydrogen bonding between $\text{Au/HS}(\text{CH}_2)_2\text{COOH}$ and $\text{CH}_3(\text{CH}_2)_{12}\text{COOH}$. The band at 1722 cm^{-1} in Figure 1b has been assigned to the C=O stretching vibration for a laterally hydrogen-bonded carboxylic acid terminal group, as shown in Scheme II (15,16). After $\text{CH}_3(\text{CH}_2)_{12}\text{COOH}$ exposure, the band shifts to 1717 cm^{-1} (Figure 1a). It has been shown previously that a 16 cm^{-1} shift in the C=O stretching frequency of *n*-alkanoic acids from about 1726 to 1710 cm^{-1} corresponds to a structural change from laterally hydrogen-bonded to a face-to-face dimer configuration (15,17). Based on the observed frequency shift of 5 cm^{-1} , we propose a model in which adsorbed $\text{CH}_3(\text{CH}_2)_{12}\text{COOH}$ is hydrogen-bonded to surface-confined $\text{HS}(\text{CH}_2)_2\text{COOH}$ in both face-to-face and lateral configurations; that is, a dynamic superposition of the two configurations shown at the bottom of Scheme II.

Proton Transfer Reactions. Figure 2 presents FTIR-ERS spectra for a $\text{Au/HS}(\text{CH}_2)_{10}\text{COOH}$ monolayer after and before exposure to a saturated vapor of $\text{CH}_3(\text{CH}_2)_9\text{NH}_2$. Before amine exposure (Figure 2b), the asymmetric and symmetric C-H stretching vibrations, which arise from the methylene groups in the $\text{Au/HS}(\text{CH}_2)_{10}\text{COOH}$ monolayer, are present at 2919 and 2849 cm^{-1} , respectively. As discussed earlier, the bands at 1739 and 1718 cm^{-1} are due to the C=O stretching vibrations of non-hydrogen-bonded and laterally hydrogen-bonded

COOH terminal groups, respectively. The absence of a high-energy O-H stretching band is consistent with prior studies of acids in solid-state-like environments (15,19), and the effect may be compounded in the present case by an orientation effect.

The COOH-terminated monolayer surface recognizes vapor-phase $\text{CH}_3(\text{CH}_2)_9\text{NH}_2$, as indicated in Figure 2a by the increased intensity of the methylene stretching bands at 2921 and 2853 cm^{-1} , and the appearance of the asymmetric and symmetric methyl vibrations at 2966 and 2879 cm^{-1} , respectively. Importantly, the C=O band at 1739 cm^{-1} (Figure 2b), which corresponds to non-hydrogen-bonded COOH groups, disappears after amine exposure while most of the C=O band intensity at 1718 cm^{-1} , which corresponds to laterally hydrogen-bonded COOH groups, remains and shifts slightly to 1715 cm^{-1} (20). On the basis of these data, we conclude that non-hydrogen-bonded C=O groups undergo a proton transfer reaction with NH_2 groups. This conclusion is supported by the disappearance of the C=O stretching band at 1739 cm^{-1} and bands traceable to COO^- (1610 cm^{-1} , ν_{COO^-}) and NH_3^+ (1506 cm^{-1} , $\delta_{\text{NH}_3^+}$) groups in Figure 2a. Since gravimetric measurements indicate that the surface coverage of $\text{CH}_3(\text{CH}_2)_9\text{NH}_2$ is about one monolayer, laterally hydrogen-bonded COOH groups, which are represented by the band at 1718 cm^{-1} , must undergo a hydrogen bonding interaction with $\text{CH}_3(\text{CH}_2)_9\text{NH}_2$. This conclusion is supported by the slight decrease in the C=O stretching frequency noted for hydrogen-bonded COOH groups after amine exposure (20).

The FTIR-ERS spectrum shown in Figure 2a does not exhibit noticeable change for at least 10 h, indicating that the bilayer structure formed after amine exposure is quite stable. This result is in contrast to the hydrogen-bonded bilayers, which are stable for much shorter periods.

Physical Interactions Between Probe Molecules and SAMs. In addition to chemical interactions between monolayers and molecules, we have recently begun to evaluate approaches for studying physical recognition. Our principal strategy for implementing size and shape recognition, which was originally proposed by Sagiv more than a decade ago (21,22), is shown in Scheme III. Here, template molecules possessing the same geometrical properties as the molecules to be recognized are used to define interaction sites. The inert, self-assembling *n*-alkanethiol framework isolates template-induced physical recognition sites from one another. Template molecules may or may not be removed from within the framework depending upon the nature of the experiment. Finally, the template molecules can be dispersed on the substrate prior to the framework, or they may be simultaneously codeposited. We used the latter approach.

There are a few indirect methods for characterizing molecule-size physical recognition sites, such as examining the extent of monolayer penetration by probe molecules as a function of their van der Waals radii and other chemical and physical properties (Scheme III, Frame 4). We have used an electrochemical version of this approach, which assumes that the defect sites define an array of ultramicro-electrodes, to analyze our composite SAMs (Scheme IV). In these experiments, the shape of the cyclic voltammetric wave is correlated to the size and number density of sites through which the probe molecules can penetrate, as shown on the right side of Scheme IV (6).

Chemical Characterization. The cyclic voltammetry results shown in Figure 3 were obtained from an electrode prepared by soaking Au foils in ethanol solutions containing various ratios of the defect-inducing organomercaptan template $\text{HS}(\text{C}_6\text{H}_4)\text{OH}$, 4-HTP, and the framework *n*-alkanethiol $\text{HS}(\text{CH}_2)_{15}\text{CH}_3$, C_{16}SH . Following deposition of the composite monolayer, we cycled the electrode potential

between +0.3 and -0.5 V at 0.1 V/s in an aqueous electrolyte solution consisting of 5 mM $\text{Ru}(\text{NH}_3)_6^{3+}$ and 1.0 M KCl. In the presence of defect sites that have the correct combination of size and intermolecular interaction energies, the $\text{Ru}(\text{NH}_3)_6^{3+}$ probe molecules should penetrate the inert framework and undergo electron exchange with the underlying Au surface. If probe molecules cannot penetrate the monolayer framework, then they can only be reduced by electrons that tunnel through the C_{16}SH layer. Since the distance of closest approach of the probe to the electrode surface is approximately the thickness of the monolayer, about 21 Å, the tunneling current should be small relative to that arising from direct electron transfer at template-induced defect sites.

Figure 3a shows the result obtained for a nominally defect-free C_{16}SH monolayer surface. The roughly exponential shape of the cyclic voltammogram and the magnitude of the maximum cathodic current are consistent with electron tunneling through the film (23,24). Figure 3b shows the behavior of an electrode modified in a solution containing 4-HTP and C_{16}SH present in a 1:1 ratio. Several points are noteworthy. First, the maximum cathodic current is about five times higher than that of the completely passivated electrode. We ascribe this current increase to surface defects induced by the template molecules; that is, the defects permit $\text{Ru}(\text{NH}_3)_6^{3+}$ to penetrate the monolayer framework. Second, the shape of the cyclic voltammogram is approximately sigmoidal, rather than exponential, and similar to that expected for an array of microelectrodes (25). This suggests that the template-induced defects are small and widely spaced relative to the diffusion layer thickness, since either large defects or closely-spaced small defects will result in peak-shaped cyclic voltammograms that are characteristic of linear diffusion (Scheme IV). Third, since the concentrations of template and framework molecules in the deposition solution are identical, and since it is clear that only a very small fraction of the molecules on the Au surface are template molecules, it follows that the much longer framework molecules compete more effectively for surface adsorption sites than the template molecules.

Figures 3c and 3d are consistent with the qualitative interpretation of Figure 3b. The shapes of these voltammograms arise from radial diffusion of $\text{Ru}(\text{NH}_3)_6^{3+}$ to small, widely dispersed defect sites on the electrode surface. This conclusion is confirmed by the scan rate dependence of the data shown in Figure 3d: scan rates between 10 and 1000 mV/s result in only a doubling of the maximum limiting current, i_{lim} , which is not consistent with the ten-fold increase anticipated for linear diffusion (26). As the concentration of the template molecules in the deposition solution is increased relative to the framework molecules, i_{lim} increases and there is a clear departure from pure radial diffusion into a mixed linear/radial regime. Mixed diffusion behavior is especially evident in Figure 3e, but when 4-HTP/ C_{16}SH = 15, nearly ideal linear diffusion obtains (Figure 3f). When 4-HTP/ C_{16}SH = 30, the cyclic voltammetry obtained using the modified surface (Figure 3g) is indistinguishable from that of a naked Au surface (Figure 3h).

Figure 4 presents data analogous to those shown in Figure 3, except that the solution-phase redox probe molecule is $\text{Fe}(\text{CN})_6^{3-}$. This set of data follows the general trends discussed for Figure 3. For example, there is a clear progression from electron transfer via tunneling through the monolayer film to direct electron transfer at the electrode surface governed first by radial, and then by linear, diffusion as the 4-HTP/ C_{16}SH ratio increases. Qualitatively, the only difference between the cyclic voltammograms shown in Figures 3 and 4 is that the transition from radial to linear diffusion occurs at a higher 4-HTP/ C_{16}SH value for $\text{Fe}(\text{CN})_6^{3-}$ than for $\text{Ru}(\text{NH}_3)_6^{3+}$. Since the perforated monolayers used to generate Figures 3 and 4 are the same there is only one possible explanation for this behavior: some of the defect sites that admit $\text{Ru}(\text{NH}_3)_6^{3+}$ do not admit $\text{Fe}(\text{CN})_6^{3-}$. That is, although the total number and average size of the defects is fixed, there are differences in the intermolecular interactions between the probe molecules and at least some of the

molecular recognition defect sites. This important observation indicates that the defect sites discriminate between probe molecules. These data also confirm that the template-induced defects are of molecular dimension; if they were not, then the shapes of the voltammograms obtained using both $\text{Ru}(\text{NH}_3)_6^{3+}$ and $\text{Fe}(\text{CN})_6^{3-}$ probe molecules would be identical.

We have used several probe molecules other than $\text{Ru}(\text{NH}_3)_6^{3+}$ and $\text{Fe}(\text{CN})_6^{3-}$ to evaluate intentionally perforated organic monolayer surfaces, and the results of these studies are summarized in Table I and Figure 5. On the basis of these data, we conclude that while the size and shape of defects is an important factor in determining the extent of probe penetration, chemical characteristics such as the permanent molecular charge, are of equal or greater importance.

Table I. Physical Properties of Probe Molecules Used in this Study.

Probe Molecule ^f	Hydrated Diameter (Å)	Diffusion Coefficient ($10^{-6} \text{ cm}^2/\text{s}$)	Heterogeneous Rate Constant (cm/s)
$\text{Mo}(\text{CN})_8^{4-/3-}$	9.0 ^a	4.8	0.5 ^b
$\text{Fe}(\text{CN})_6^{4-/3-}$	5.2	8.3 ^c	0.15 ^c
$\text{Fe}(\text{bpy})(\text{CN})_4^{2-/1-}$	5.7	7.7 ^c	0.43 ^c
$\text{Fe}(\text{bpy})_2(\text{CN})_2^{0/1+}$	10.1	4.3 ^c	0.63 ^c
$\text{Ru}(\text{NH}_3)_6^{3+/2+}$	6.2	7.1 ^d	>1 ^e

a. Otashima, K.; Kotato, M.; Sugawara, M.; Umezawa, Y. *Anal. Chem.* **1993**, *65*, 927.

b. Saji, T.; Maruyama, Y.; Aoyagui, S. *J. Electroanal. Chem.* **1978**, *86*, 219.

c. Saji, T.; Yamada, T.; Aoyagui, S. *J. Electroanal. Chem.* **1975**, *61*, 147.

d. Licht, S.; Cammarata, V.; Wrighton, M. S. *J. Phys. Chem.* **1990**, *94*, 6133.

e. Endicott, J. F.; Schroeder, R. R.; Chidester, D. H.; Ferrier, D. R. *J. Phys. Chem.* **1973**, *77*, 2579.

f. (bpy) is the bipyridyl ligand.

Scanning Tunneling Microscope Characterization. The electrochemical approach just described is clearly an important means for evaluating template-induced defects, but the results are difficult to interpret in terms of the purely chemical and physical characteristics of the defect sites. Clearly, a more direct approach for visualizing defects is desirable. We have attempted to use scanning tunneling microscopy (STM) to directly image template-induced defects, but our results have been ambiguous for at least two reasons. First, there are many structures on the surface of SAM-covered Au substrates that appear by STM to be defect sites whether templates are present or not (27-29). We have recently shown that these features are due to monoatomic pits in the Au surface, and while not electroactive, they appear similar to intentionally formed defect sites (28). Second, we have found that the STM tip changes the structure of SAM surfaces as a function of the number of scans regardless of the imaging conditions employed (29). This effect tends to enlarge the defects rendering their initial size and shape impossible to determine.

As an alternative to direct visualization, we have considered the two indirect STM-based methods illustrated in Scheme V. The fundamental problem with imaging organic surfaces is that they are soft, and thus easily damaged by the STM tip. The two processes shown on the bottom of Scheme V avoid this problem. On the right side of Scheme V a metal is electrochemically deposited into the template-

defined structure, which creates resilient positive images of the original defects. This approach is promising, but there are a number of technical difficulties that make data interpretation difficult at the present time (30). A less ambiguous approach is shown on the left side of Scheme V. Here, we use electrochemical methods to etch the Au substrate only in those regions that contain a suitable template molecule. While this approach permits us to evaluate the number density of defects and their size after etching, it does not permit us to directly evaluate the defect size prior to etching. We now present our preliminary findings concerning the etching method.

In preparation for using this combined STM/CN⁻-etching method to study intentionally perforated monolayers, we correlated the electrochemical response obtained from SAMs containing etched adventitious defects to data calculated from STM images. We prepared C₁₆SH SAMs by soaking flame-annealed Au(111) surfaces in dilute ethanol solutions of the mercaptan for about 1 day (29,30). We then etched the SAMs three times in an aqueous 0.1 M KCN/0.1 M Na₂HPO₄ solution (etching was carried out by stepping the substrate potential to positive potentials three times: 0.15 V for 30 s, 0.20 V for 20 s, and then 0.20 V for 10 s). This process results in etching of the Au substrate only in those regions not passivated by the SAM; that is, in regions of adventitious defects. After etching, we used a NanoScope III STM (Digital Instruments, Santa Barbara, CA) to image the surface. Image analysis reveals the average size and number density of the etched defect sites.

Figure 6a shows an inverted image of an atomically flat SAM-modified Au(111) surface after etching in CN⁻. We quantitatively analyzed the etched surface by counting the number density of pits and measuring their average radius in several different locations. We found that the average defect radius was 6.8 ± 1.6 nm. The number density of defects was $0.9 \times 10^9/\text{cm}^2$, which is in good agreement with our prior results obtained using a less direct electrochemical method (6).

We performed cyclic voltammetric analyses for the etched surface shown in Figure 6a. These data, which are shown in Figure 6b, were obtained by immersing the electrode in an electrolyte solution consisting of 5 mM Ru(NH₃)₆³⁺ and 1.0 M KCl and then measuring the resulting current over the potential range 0.3 to -0.5 V (vs. Ag/AgCl). The value of i_{lim} is nearly independent of scan rate, indicating good ultramicroelectrode behavior, and the sigmoidal shape indicates that the diffusion layers of the electrodes do not overlap significantly (6). We compared the experimentally determined value of i_{lim} , 0.5 μA , to the value calculated from the STM image, 4.8 μA , using the relationship given in eq 1 for the limiting current at a very small disk electrode. Here, n = 1 eq/mol, F is the Faraday, r is the average defect radius, p is the total number of defects, D is the diffusion coefficient of

$$i_{\text{lim}} = 4nFrDCp \quad (1)$$

Ru(NH₃)₆³⁺, and C is its concentration. It is interesting and somewhat disconcerting to note that the calculated and electrochemically measured values of i_{lim} differ by approximately one order of magnitude. At the present time we believe this is a consequence of four factors: (1) the etch pits are shaped more like cylinders than disks, so eq 1 is not the best expression to use for calculating a theoretical value of i_{lim} ; (2) if the factors that govern diffusion to nanometer-scale electrodes are not the same as those that govern diffusion to electrodes of micron-scale dimensions, then eq 1 is inappropriate (31); (3) some of the etch pits (or a portion of all or some of the etch pits) observed by STM may not be electroactive; (4) if there is communication between etch pits, then the electrochemically measured value of i_{lim} will be suppressed. We are presently considering all of these possibilities in order to reconcile the STM and electrochemical data. Qualitatively,

however, we believe this method is useful for correlating the number of molecule-sized, template-induced defects to electrochemical results. Indeed, our preliminary studies of 4-HTP-induced defects show that higher concentrations of 4-HTP in the deposition solution result in STM images containing higher surface concentrations of etch pits.

Conclusions

We have shown that SAMs can be used to construct organic surfaces that discriminate between probe molecules on the basis of their chemical and physical characteristics. While our current interest is in studying the fundamental interactions that exist between monolayers and molecules that lead to this level of discrimination, our ultimate goal is to combine two or more chemical or physical interaction phenomena into individual recognition sites. Analysis of these more complex structures will lead to a better understanding of how individual interactions combine in natural systems to yield highly specific binding sites.

Acknowledgments

We gratefully acknowledge the Office of Naval Research and the National Science Foundation (CHE-90146566) for supporting this work. We also thank Dr. Antonio J. Ricco of Sandia National Laboratories for helpful discussions, insightful comments, and data obtained using surface acoustic wave devices that support the findings presented herein. JKS acknowledges an IBM Manufacturing Research Fellowship.

Literature Cited

1. Wulff, G. In *Polymeric Reagents and Catalysts*; Ford, W. T., Ed.; ACS Symposium Series 308; American Chemical Society: Washington, D.C., 1986; pp 186-230, and references therein.
2. Lehn, J.-M. *Angew. Chem. Int. Ed. Engl.* **1990**, *29*, 1304.
3. Rebek, J. Jr. *Acc. Chem. Res.* **1990**, *23*, 399.
4. Nuzzo, R. G.; Allara, D. L. *J. Am. Chem. Soc.* **1983**, *105*, 4481.
5. Dubois, L. H.; Nuzzo, R. G. *Annu. Rev. Phys. Chem.* **1992**, *43*, 437, and references therein.
6. Chailapakul, O.; Crooks, R. M. *Langmuir* **1993**, *9*, 884.
7. Chidsey, C. E. D.; Loiacono, D. N. *Langmuir* **1990**, *6*, 682.
8. Creager, S. E.; Hockett, L. A.; Rowe, G. K. *Langmuir* **1992**, *8*, 854.
9. Sun, L.; Johnson, B.; Wade, T.; Crooks, R. M. *J. Phys. Chem.* **1990**, *94*, 8869.
10. Sun, L.; Thomas, R. C.; Crooks, R. M.; Ricco, A. J. *J. Am. Chem. Soc.* **1991**, *113*, 8550.
11. Kepley, L. J.; Crooks, R. M.; Ricco, A. J. *Anal. Chem.* **1992**, *64*, 3191.
12. Sun, L.; Kepley, L. J.; Crooks, R. M. *Langmuir* **1992**, *8*, 2101.
13. Sun, L.; Crooks, R. M.; Ricco, A. J., *Langmuir* **1993**, *9*, 1775.
14. Xu, C.; Sun, L.; Kepley, L. J.; Crooks, R. M. *Anal. Chem.* **1993**, *65*, 2102.
15. Nuzzo, R. G.; Dubois, L. H.; Allara, D. L. *J. Am. Chem. Soc.* **1991**, *112*, 558.
16. Ihs, A.; Liedberg, B. *J. Colloid Interface Sci.* **1991**, *144*, 282.
17. Yarwood, J. *Spectroscopy* **1990**, *5*, 34.
18. Chidsey, C. E. D.; Loiacono, D. N. *Langmuir* **1990**, *6*, 682.
19. Bellamy, L. J. *The Infra-red Spectra of Complex Molecules*, 3rd ed., Chapman and Hall: London, 1975.

20. Vinogradov, S. N.; Linnell, R. H. *Hydrogen Bonding*; Van Nostrand Reinhold Co.: New York, 1971; p 74.
21. Sagiv, J. *Isr. J. Chem.* **1979**, *18*, 339.
22. Sagiv, J. *Isr. J. Chem.* **1979**, *18*, 346.
23. Chidsey, C. E. D. *Science* **1991**, *251*, 919.
24. Finklea, H. O.; Hanshew, D. D. *J. Am. Chem. Soc.* **1992**, *114*, 3173.
25. Wightman, R. M.; Howell, J. O. *Anal. Chem.* **1984**, *56*, 524.
26. Bard, A. J.; Faulkner, L. R. *Electrochemical Methods*; Wiley: New York, 1980; p 222.
27. Sun, L.; Crooks, R. M. *Langmuir* **1993**, *9*, 1775.
28. Chailapakul, O.; Sun, L.; Xu, C.; Crooks, R. M. *J. Am. Chem. Soc.*, in press.
29. Ross, C. B.; Sun, L.; Crooks, R. M. *Langmuir* **1993**, *9*, 632.
30. Sun, L.; Crooks, R. M. *J. Electrochem. Soc.* **1991**, *138*, L23.
31. Smith, C. P.; White, H. S. the University of Utah, personal communication.

Figure 1. FTIR-ERS spectra of a Au/HS(CH₂)₂COOH surface before (b) and after (a) exposure to vapor-phase CH₃(CH₂)₁₂COOH and FTIR-ERS spectra of a Au/HS(CH₂)₂CH₃ surface before (d) and after (c) exposure to vapor-phase CH₃(CH₂)₁₂COOH.

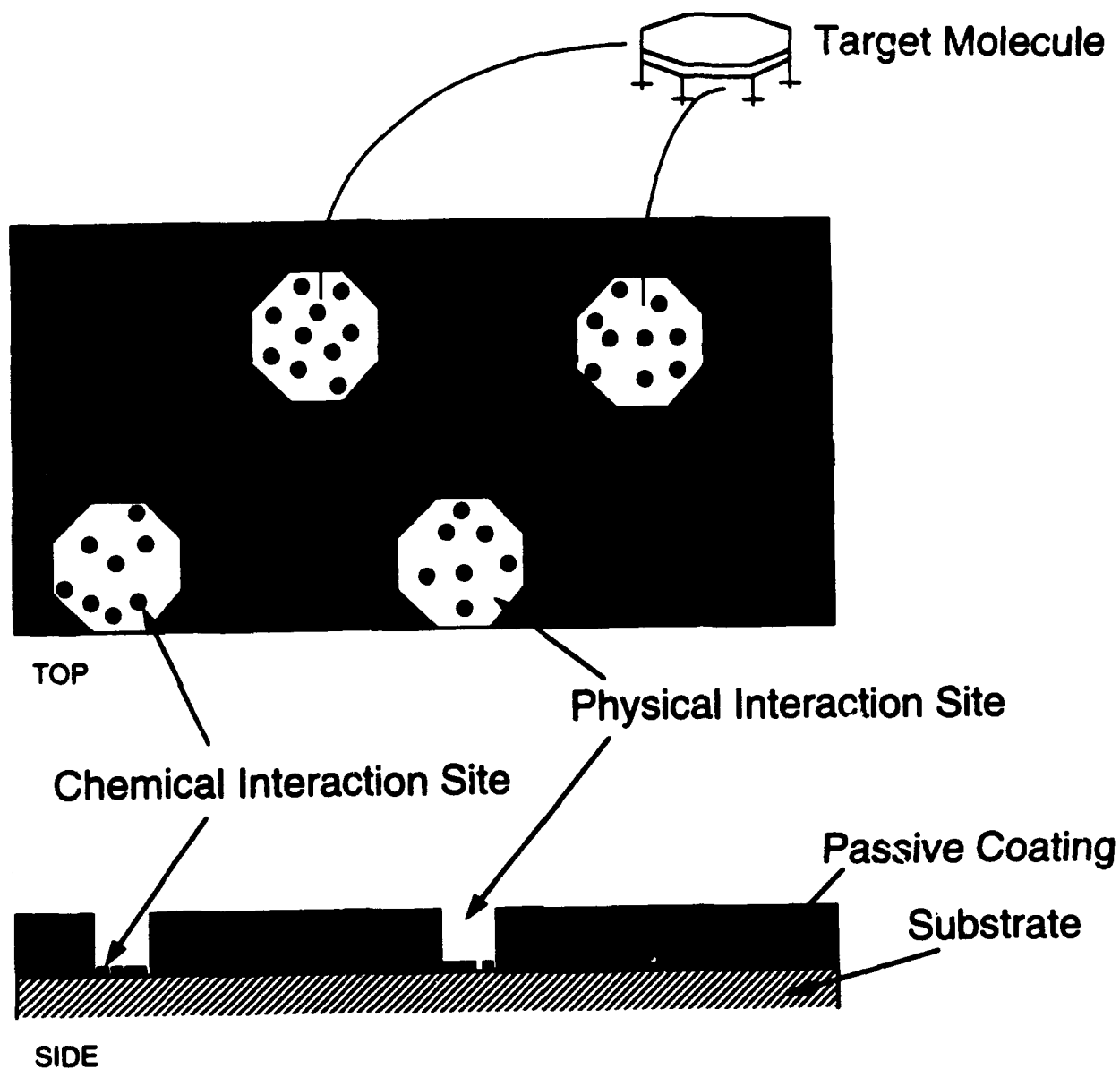
Figure 2. FTIR-ERS spectra of a Au/(CH₂)₁₀COOH monolayer before (b) and after (a) exposure to vapor-phase CH₃(CH₂)₉NH₂.

Figure 3. Cyclic voltammograms obtained for perforated, composite monolayers formed by immersing a Au surface into ethanol solutions containing various ratios of 4-HTP/C₁₆SH. The data were obtained in an aqueous electrolyte solution consisting of 5 mM Ru(NH₃)₆³⁺ and 1.0 M KCl. The scan rate was 0.1 V/s.

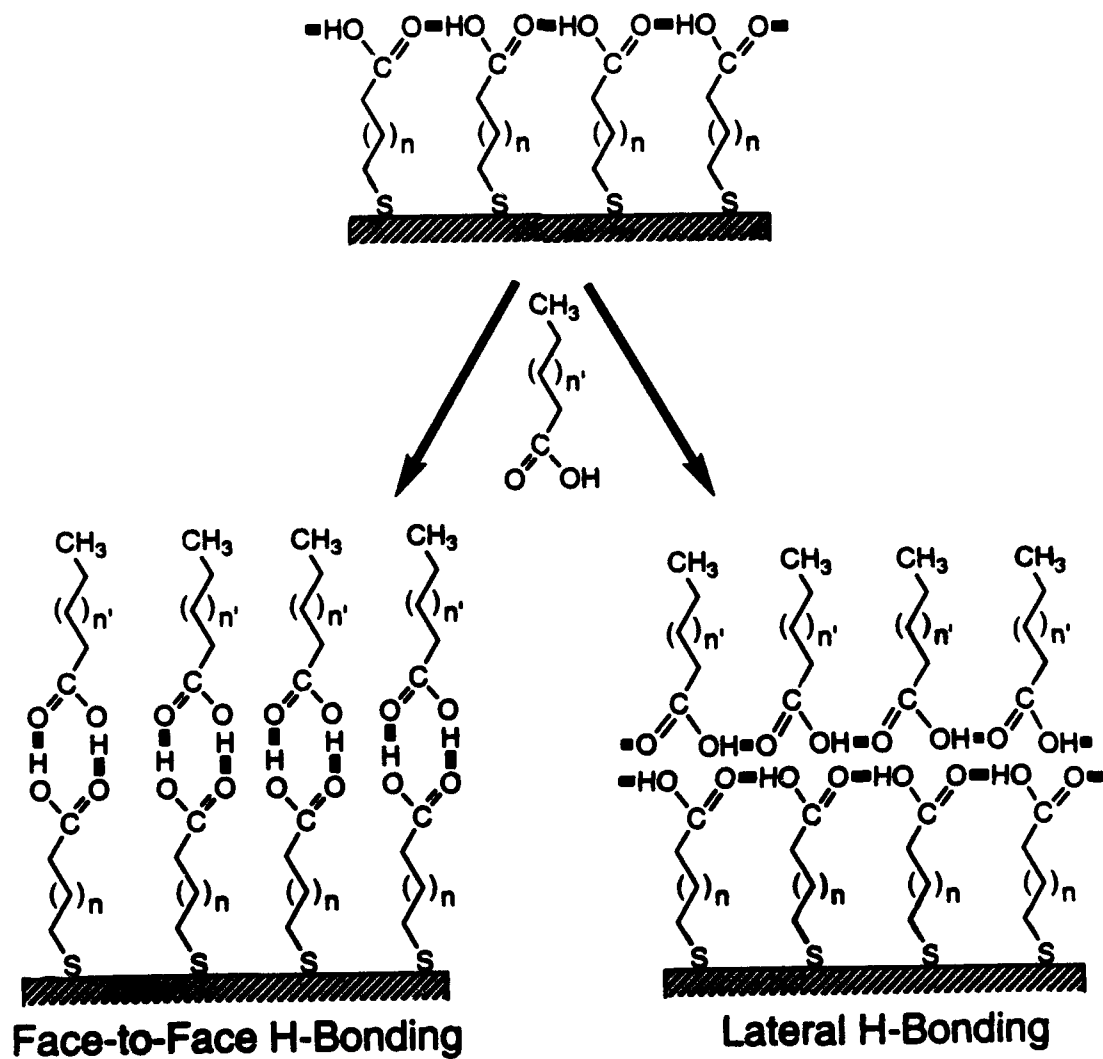
Figure 4. Cyclic voltammograms for perforated, composite monolayers formed by immersing a Au surface in ethanol solutions containing various ratios of 4-HTP/C₁₆SH. The data were obtained in an aqueous electrolyte solution consisting of 5 mM Fe(CN)₆³⁻ and 1.0 M KCl. The scan rate was 0.1 V/s.

Figure 5. Cyclic voltammograms for a perforated, composite monolayer formed by immersing a Au surface in an ethanol solution containing a ratio of 4-HTP/C₁₆SH = 5. The data were obtained in aqueous electrolyte solutions containing 1.0 M KCl and the indicated probe molecules. Cyclic voltammograms were obtained in the sequence given in the figure; data for Ru(NH₃)₆³⁺ were obtained after each of the other probe molecules to insure that the characteristics of the modified electrode surface did not change during the course of the experiment. The scan rate was 0.1 V/s. Some properties of the probe molecules are given in Table I.

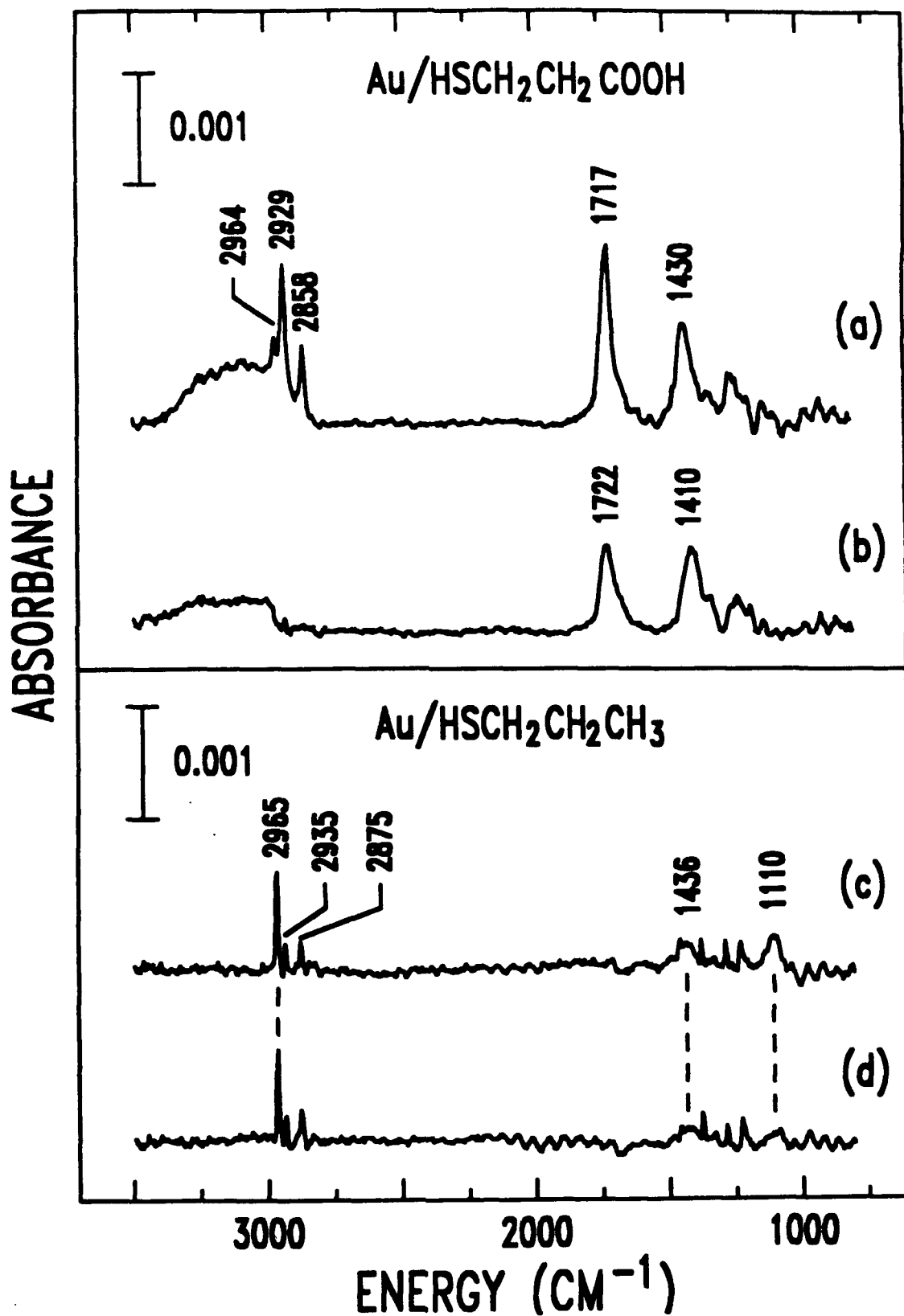
Figure 6. (a) STM image of a C₁₆SH SAM containing adventitious defects obtained after CN⁻ etching. The image is inverted on the axis normal to the surface to emphasize the size, number density, and depth of the etch pits (note that the vertical axis is expanded relative to the two horizontal axes). The tip/substrate bias was +300 mV and the tunneling current was 150 pA. (b) Cyclic voltammograms obtained in a 5 mM Ru(NH₃)₆³⁺/1.0 M KCl aqueous solution. The electrode area was 6 x 10⁻⁴ cm² and the scan was made between 0.3 and -0.5 V.

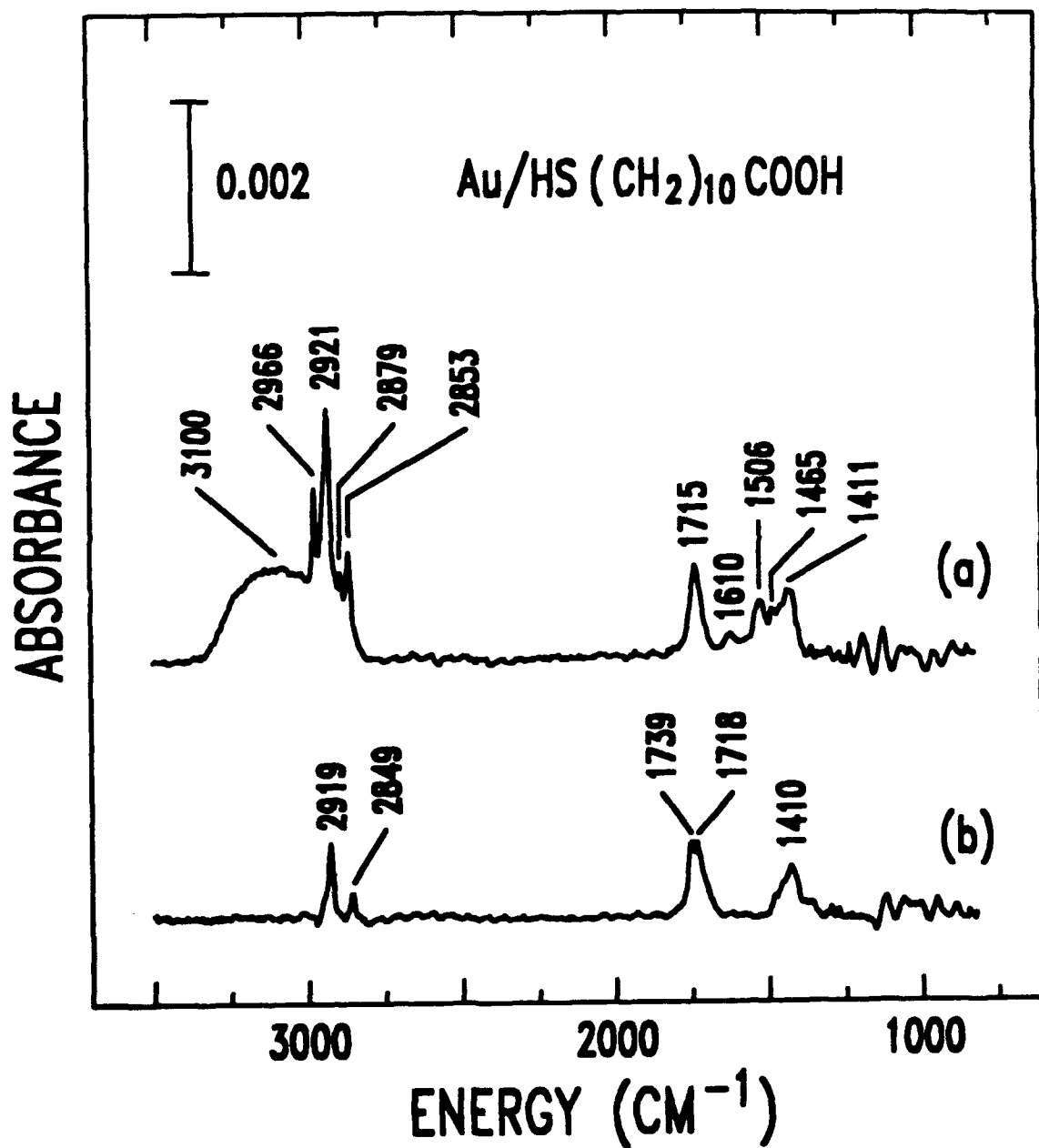


Scheme 1/Crooks et al.
(Bottom Right Corner)

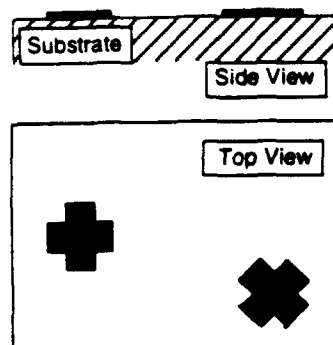


Scheme II/Crooks et al.
(Bottom Right Corner)

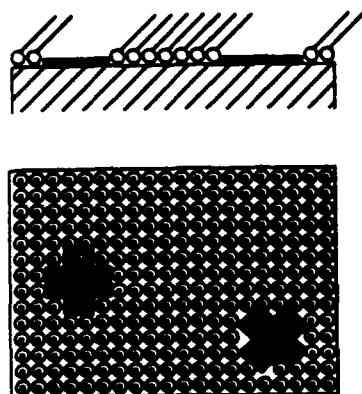




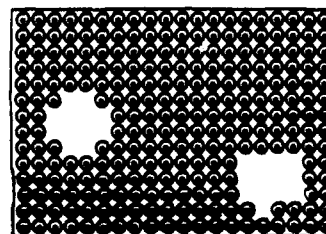
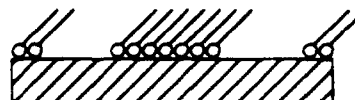
1. Template Adsorption



2. Framework Adsorption



3. Template Desorption



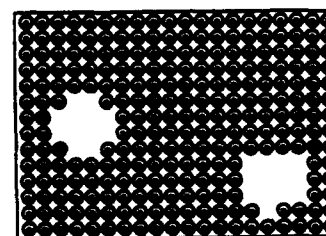
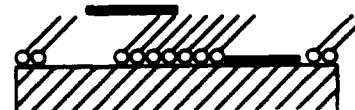
4a.

Discrimination

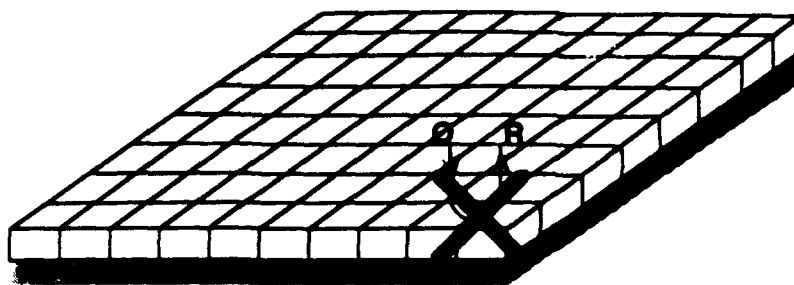


4b.

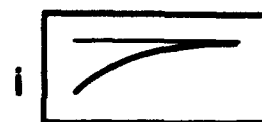
Recognition



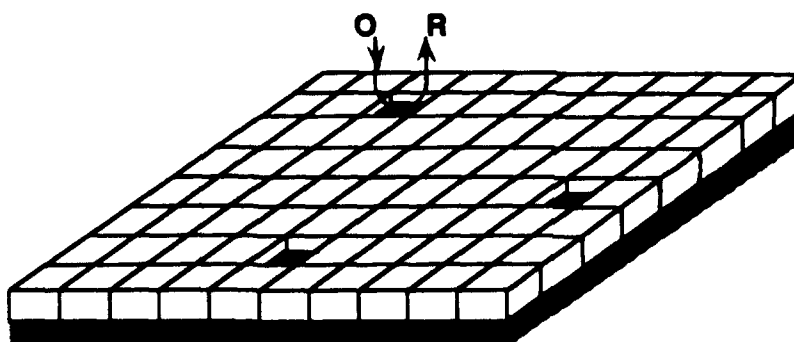
Scheme III/Crooks et al.
(Bottom Right Corner)



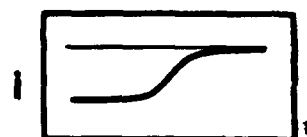
**Framework only
No defects**



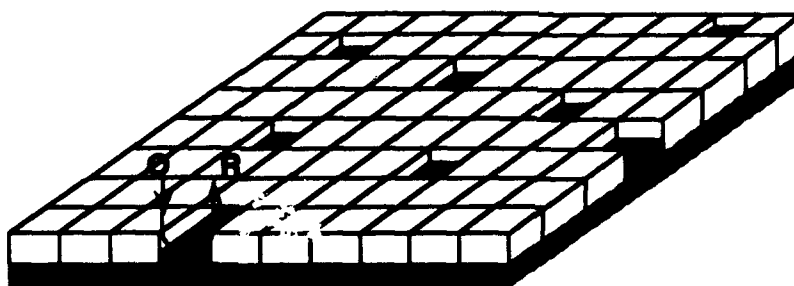
E



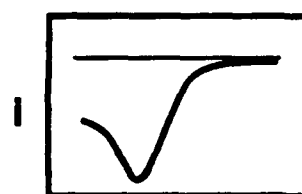
**Low Template : Framework Ratio
Low defect density**



E



**High Template : Framework Ratio
High defect density**



E



= Framework



= Template

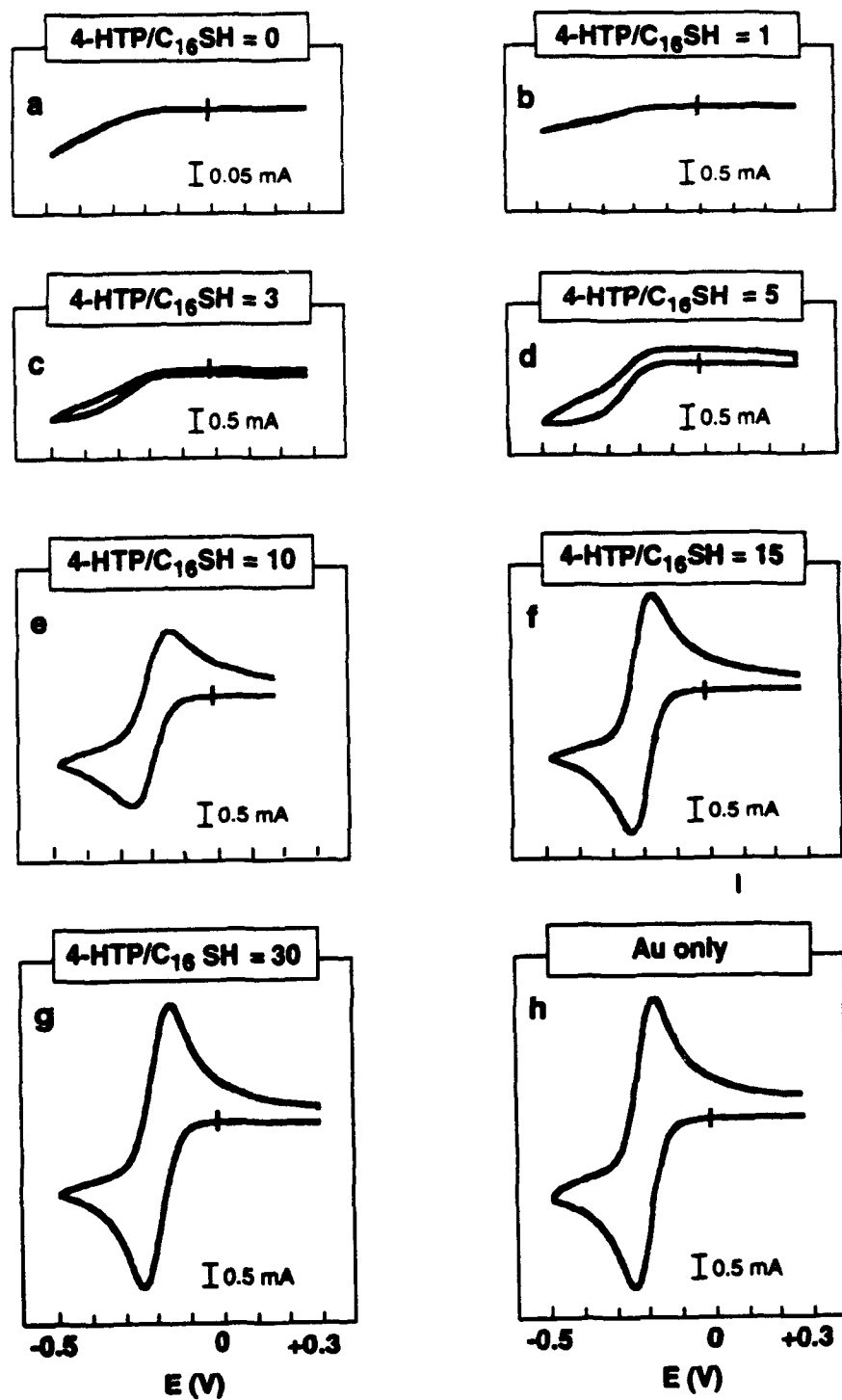


Figure 3/Crooks et al.
(Bottom Right Corner)

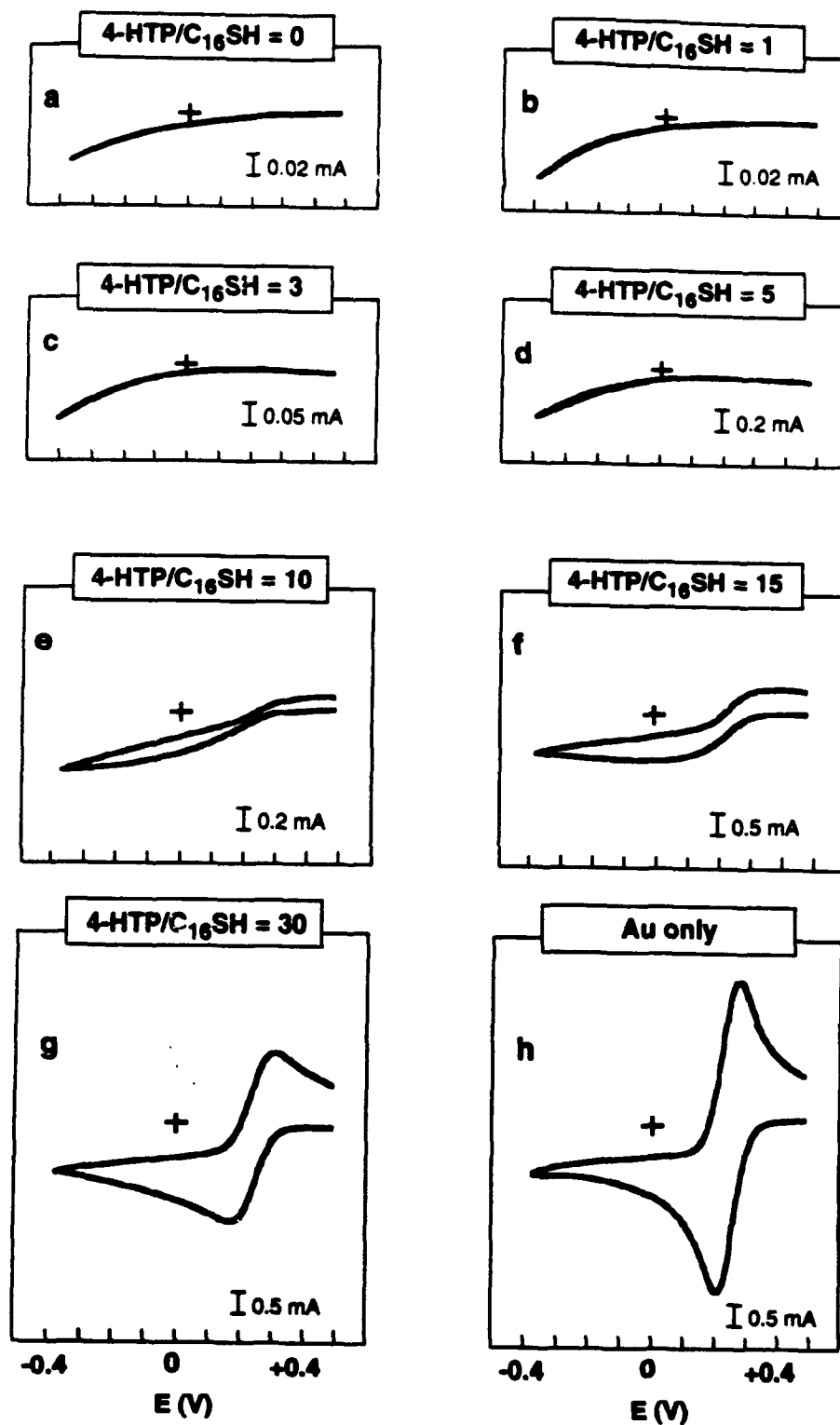


Figure 4/Crooks et al.
(Bottom Right Corner)

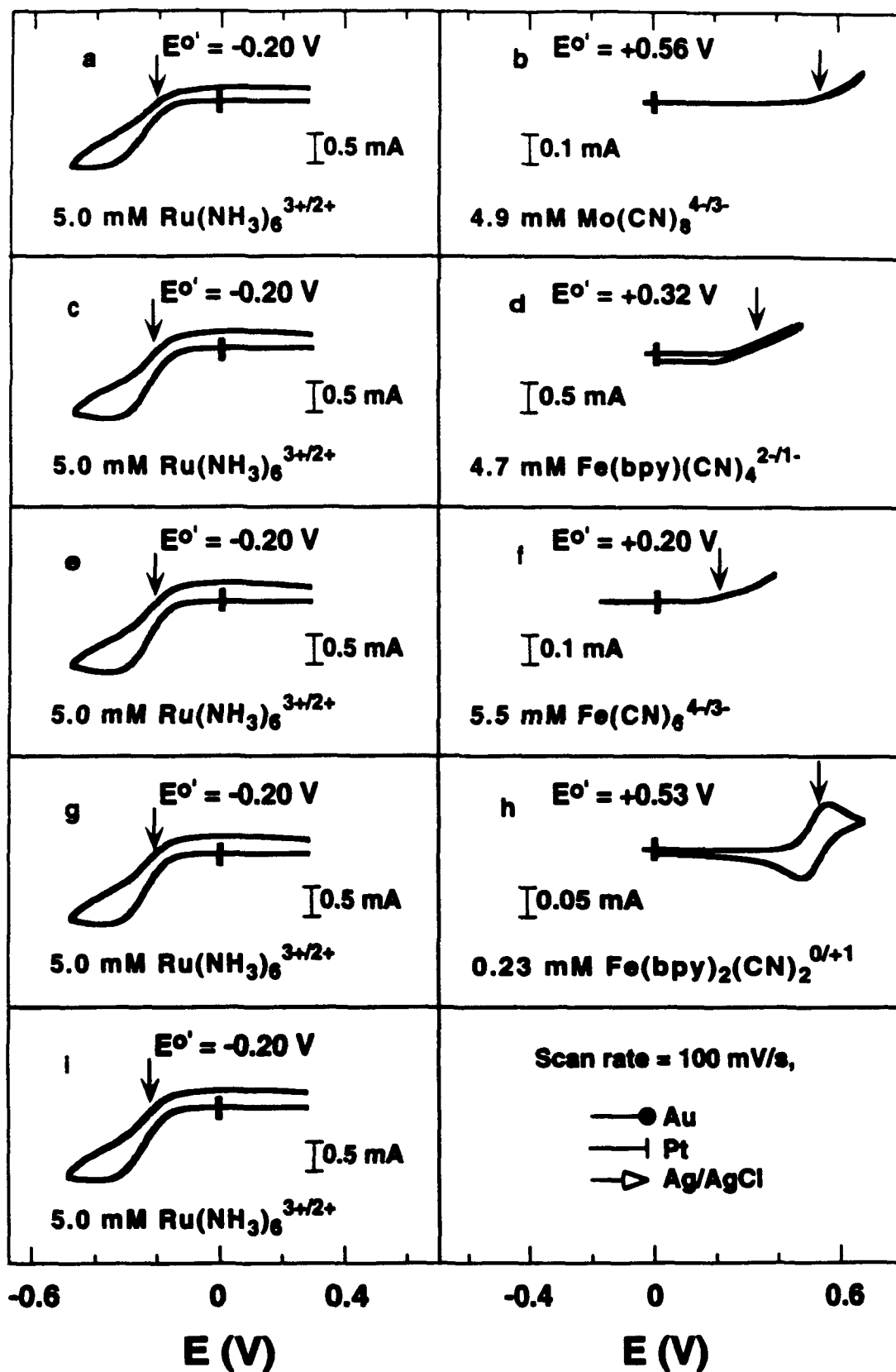


Figure 5/Crooks et al.
 Bottom Right Corner

